A Lagrangian investigation of the small-scale features of turbulent entrainment through particle tracking and direct numerical simulation

MARKUS HOLZNER[1,2]†, A. LIBERZON[1,3], N. NIKITIN[4],
B. LÜTHI[1,2], W. KINZELBACH[1,2] AND A. TSINOBER[1,3,5]

[1]International Collaboration for Turbulence Research
[2]Institute of Environmental Engineering, ETH Zurich, Wolfgang-Pauli-Str. 15, 8093 Zurich, Switzerland
[3]School of Mechanical Engineering, Faculty of Engineering, Tel Aviv University, Tel Aviv 69978, Israel
[4]Institute of Mechanics, Moscow State University, 119899 Moscow, Russia
[5]Institute for Mathematical Sciences and Department of Aeronautics, Imperial College,
SW7 2AZ London, UK

We report an analysis of small-scale enstrophy ω^2 and rate of strain s^2 dynamics in the proximity of the turbulent/non-turbulent interface in a flow without strong mean shear. The techniques used are three-dimensional particle tracking (3D-PTV), allowing the field of velocity derivatives to be measured and followed in a Lagrangian manner, and direct numerical simulations (DNS). In both experiment and simulation the Taylor-microscale Reynolds number is $Re_\lambda = 50$. The results are based on the Lagrangian viewpoint with the main focus on flow particle tracers crossing the turbulent/non-turbulent interface. This approach allowed a direct investigation of the key physical processes underlying the entrainment phenomenon and revealed the role of small-scale non-local, inviscid and viscous processes. We found that the entrainment mechanism is initiated by self-amplification of s^2 through the combined effect of strain production and pressure–strain interaction. This process is followed by a sharp change of ω^2 induced mostly by production due to viscous effects. The influence of inviscid production is initially small but gradually increasing, whereas viscous production changes abruptly towards the destruction of ω^2. Finally, shortly after the crossing of the turbulent/non-turbulent interface, production and dissipation of both enstrophy and strain reach a balance. The characteristic time scale of the described processes is the Kolmogorov time scale, τ_η. Locally, the characteristic velocity of the fluid relative to the turbulent/non-turbulent interface is the Kolmogorov velocity, u_η.

1. Introduction

An important feature of many turbulent flows is the sharp interface that exists between turbulent and surrounding non-turbulent flow regions. Examples of such flows are free shear flows (jets, plumes, wakes, mixing layers), penetrative convection in the atmosphere and in the ocean, gravity currents, avalanches and clear air turbulence. An interesting property of these flows, commonly referred to as *turbulent entrainment*,

† Present address: ETH Hönggerberg, Wolfgang-Pauli-Str. 15, Zurich, Switzerland.

is the process of transition of fluid from a non-turbulent to turbulent state through the boundary between the two regions (e.g. Tsinober 2001). One physically qualitative distinction between turbulent and non-turbulent regions is that turbulent regions are rotational, whereas the non-turbulent ones are practically irrotational (Corrsin 1943; Corrsin & Kistler 1954). Until recently it was difficult to use this distinction effectively, since it requires information on small-scale vorticity, which was difficult to access experimentally. Also for this reason, the understanding of the mechanics of turbulent/non-turbulent interfaces and the associated entrainment process is still incomplete. Also, since turbulent entrainment is a phenomenon of Lagrangian nature, the Lagrangian frame of reference is the appropriate one to investigate the details of its mechanism. However, until now experimental studies of this kind are essentially lacking in the literature.

In an early study, Corrsin & Kistler (1954) proposed on the basis of dimensional reasoning that the thickness of the turbulent interface (they called it the 'viscous sublayer') and its propagation speed are determined by molecular viscosity, ν, and the mean-square rate of straining in the adjacent turbulent layer, which is proportional to ϵ/ν, where ϵ is the energy dissipation in the adjacent turbulent region. On dimensional grounds, the thickness of the interface is then proportional to the Kolmogorov length scale $\eta = (\nu^3/\epsilon)^{1/4}$ and its speed of advance to the Kolmogorov velocity scale $u_\eta = (\epsilon\nu)^{1/4}$. However, at large Reynolds numbers, the entrainment rate and the propagation velocity of the interface relative to the fluid are known to be independent of viscosity (e.g. Tritton 1988; Tsinober 2001; Hunt, Eames & Westerweel 2006). Therefore, the slow process of diffusion of vorticity into the ambient fluid must be accelerated by interaction of velocity fields of eddies of all sizes, from viscous eddies to the energy-containing eddies so that the overall rate of entrainment is set by large-scale parameters of the flow. This means that although the spreading is brought about by small eddies (viscosity), its rate is governed by larger eddies. The total area of the interface, over which the spreading is occurring at any instant, is determined by these larger eddies (Tritton 1988).

The progress in experimental techniques and computational methods over the last few decades has shed more light on the processes at work. For example, some effort was dedicated to elucidating the significance of small-scale motion for the entrainment process compared to the contribution of large scales. Bisset, Hunt & Rogers (2002) used direct numerical simulations (DNS) of a plane wake, pointing to the significance of large eddies for the observed interface dynamics. Westerweel *et al.* (2002, 2005) used fluorescent dye to detect the turbulent front and particle image velocimetry (PIV) for the analysis of flow properties at the interface of a jet. Their results indicate that small-scale eddying motion at the interface is important for its spreading. A similar view is supported by the numerical work of Mathew & Basu (2002), who analysed the process of growth of vorticity and concentration in initially non-turbulent fluid by computing pathlines of a representative collection of particles. Interesting spectral vorticity and Lagrangian velocity measurements in jets by acoustic scattering techniques are reported in Poulain *et al.* (2004). Hunt *et al.* (2006) reviewed different studies of interfacial layers adjacent to layers with weak and strong mean shear and it was shown that mean shear and anisotropy affect the characteristics of interfacial layers. For example, mean shear was reported to increase the degree of inhomogeneity, which is an intrinsic property of interfacial regions. One aim of the presented research was to isolate other important physical processes at work and the focus is on a turbulent interface in a flow without significant mean shear.
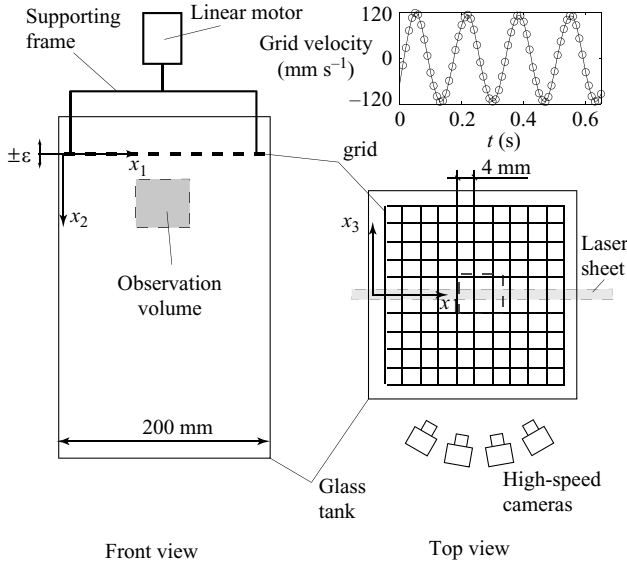
FIGURE 1. Schematic of the experimental setup. A time sample of the grid velocity obtained from the encoder signal is shown in the upper right corner.

In their recent short publication, Holzner *et al.* (2007) analysed the dependence of small-scale quantities on the distance to a turbulent/non-turbulence interface induced by planar forcing. They used three-dimensional-particle tracking (3D-PTV) and DNS to reveal some aspects of the inherent differences and the complex interplay between small-scale strain and enstrophy in the proximity of interfaces. The present paper is an extension of that work and presents an analysis of quantities in a Lagrangian frame of reference by using the same setup and techniques. The particular focus is on flow particles initially located in irrotational flow regions, which cross the boundary between nearly irrotational and turbulent flow regions, in the following called the *turbulent/non-turbulent interface*. This allowed us to identify how and when the different physical processes set in. We discuss the evolution along particle trajectories of all the terms of the balance equation for enstrophy, written as

$$\frac{\mathrm{D}}{\mathrm{D}t}\frac{\omega^2}{2} = \omega_i\omega_j s_{ij} + \nu\omega_i\nabla^2\omega_i \tag{1.1}$$

and rate of strain,

$$\frac{\mathrm{D}}{\mathrm{D}t}\frac{s^2}{2} = -s_{ij}s_{jk}s_{ki} - \tfrac{1}{4}\omega_i\omega_j s_{ij} - s_{ij}\frac{\partial^2 p}{\partial x_i \partial x_j} + \nu s_{ij}\nabla^2 s_{ij}. \tag{1.2}$$

In §2 we describe the details of the experimental and numerical techniques that have been used, the results are reported in §3 and finally the conclusions are drawn in §4.

2. Method

Experimentally, a turbulent/non-turbulent interface was realized by using the oscillating planar grid described in Holzner *et al.* (2006). A schematic of the experimental setup is shown in figure 1. The grid is a fine woven screen installed near the upper edge of a water-filled glass tank and it oscillates at a frequency of 6 Hz and with an amplitude of 4 mm. The scanning method of three-dimensional particle

tracking velocimetry used for the measurements is described in detail in Hoyer *et al.* (2005). 3D-SPTV is a flexible flow measurement technique based on the processing of stereoscopic images of flow tracer particles. As in Holzner *et al.* (2007), the derivatives of velocity, $\partial u_i / \partial x_j$, and Lagrangian acceleration, $\partial a_i / \partial x_j$, were calculated along particle trajectories. The Laplacian of vorticity, $\nabla^2 \boldsymbol{\omega}$, is obtained indirectly from the local balance equation of vorticity in the form $\nabla \times \boldsymbol{a} = \nu \nabla^2 \boldsymbol{\omega}$ by evaluating the term $\nabla \times \boldsymbol{a}$ from the Lagrangian tracking data, where ν is the kinematic viscosity of the fluid. Through this indirect method only one derivative in space is needed instead of three, but particle positions have to be differentiated twice in time in order to obtain Lagrangian acceleration. Measurements of particle positions are affected by noise and commonly one has to low-pass filter the trajectories in order to access quantities like acceleration (e.g. Voth *et al.* 2002; Mordant, Crawford & Bodenschatz 2004; Lüthi, Tsinober & Kinzelbach 2005). The lower the spatial resolution of the measurement, the more the position signal is affected by noise and the higher is the required over-sampling in time. The resolution in the present experiment is close to the one used in Lüthi *et al.* (2005) and the filtering procedure is the same as the one described in Appendix A of the same reference. The position signal is low-pass filtered with a cutoff frequency of 10 Hz, which is well above a position frequency signal of 3 Hz estimated from $\tau_\eta = 0.3$ s and well below 25 Hz, which with 50 Hz recording rate is the highest resolvable frequency. The number of tracked particles per frame is about 6×10^3 in a volume of $2 \times 2 \times 1.5 \, \text{cm}^3$ about 2 cm away from the grid and the mean interparticle distance Δx is about 1 mm, which is slightly above the estimated Kolmogorov length scale, $\eta = 0.6$ mm. We estimated η using $\eta = (\nu^3/\epsilon)^{1/4}$, where $\epsilon = 2\nu \langle s^2 \rangle$ is the measured dissipation ($s^2 = s_{ij} s_{ij}$ is the rate of strain and s_{ij} are the components of the rate of strain tensor). This estimate of the dissipation was verified by using the relation $\langle \delta \boldsymbol{u}(\boldsymbol{r}) \cdot \delta \boldsymbol{a}(\boldsymbol{r}) \rangle = -2\varepsilon$, proposed by Ott & Mann (2000). The estimated values of the mean dissipation derived by using the two different methods lie within a range of 20%. The Taylor microscale, λ, is about 7 mm and the estimated Kolmogorov time scale is $\tau_\eta = 0.3$ s, which is 15 times the time-interval between two volume scans, $\Delta t = 0.02$ s. In both experiment and simulation, the Taylor-microscale Reynolds number is $Re_\lambda = 50$. Unfortunately, the pressure and the viscous terms in (1.2) can at present not be obtained through PTV, but they are available in the DNS.

   DNS was performed in a box (side length $5L_1$, $3L_2$, $5L_3$) of fluid initially at rest. Random (in space and time) velocity perturbations are applied at the boundary $x_2 = 0$. The procedure of generating the boundary conditions is as follows. For a fixed time and at the discrete set of points, $x_1 = k\Delta_l$, $x_3 = m\Delta_l$ (k, m integers), each velocity component, u_i ($i = 1, 2, 3$), is calculated as $u_i = V_i \xi$, where ξ is a random number within the interval $[-1, 1]$ and V_i is a given velocity amplitude. For other times and spatial points (x_1, x_3) boundary velocities are obtained by cubic interpolation in time and bilinear interpolation in space. At each time the three boundary velocity components yield zero average value over the boundary plane. The method of boundary velocity assignment determines the velocity scale, $V = \max(V_i)$, and the length scale Δ_l. The corresponding time scale is defined as $\Delta_t = \Delta_l / V$. Together with the viscosity of the fluid, ν, these parameters define the Reynolds number $Re = V\Delta_l / \nu = 1000$ of the simulation. The Navier–Stokes equations are solved with shear-free conditions $\partial u_1 / \partial x_2 = \partial u_3 / \partial x_2 = u_2 = 0$ imposed at the boundary $x_2 = 3L_2$. Unlike Holzner *et al.* (2007), where a mixed spectral-finite-difference method was used, the numerical scheme is now finite differences in all three directions with time advancement computed by a semi-implicit Runge–Kutta method. This allowed
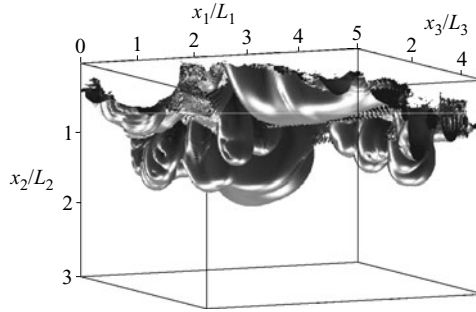
FIGURE 2. Snapshot of an enstrophy iso-surface obtained from DNS. The value of the iso-surface normalized over its mean in the turbulent region is $\omega^2/\langle\omega^2\rangle = 0.01$.

	Δx_k	Δt	Re_λ	$\tau_\eta/\Delta t$	$\eta/\Delta x_k$	$\lambda/\Delta x_k$
3D-SPTV	1 mm	0.02 s	50	15	0.6	7
DNS	$8 \times 10^{-3}\Delta_l$	$2 \times 10^{-3}\Delta_t$	50	300	2.0	28

TABLE 1. Characteristic properties of the flow for the experiment and the simulation

a straightforward implementation of the integration of Lagrangian particle paths (Nikitin 2006). The resolution is $256 \times 256 \times 256$ grid points in the x_1-, x_2- and x_3- directions. This resolution at the relatively low Reynolds number of $Re_\lambda = 50$ was necessary to obtain a simulation that is very accurate at the level of enstrophy and strain, i.e. that there is good pointwise balance between left-hand side and right-hand side of (1.1) and (1.2). The analysis is done for times when the turbulent/non-turbulent interface is about half a box size away from the source. The local Kolmogorov length scale is twice the grid spacing. The paths of 4000 fluid particles have been calculated by using

$$\frac{\mathrm{D}\boldsymbol{x}}{\mathrm{D}t} = \boldsymbol{u}(\boldsymbol{x}, t), \tag{2.1}$$

where $\boldsymbol{x}$ is the position of the fluid particle at time t. For the time integration of the particle position a third-order explicit Runge–Kutta scheme was used. The velocity and other quantities of interest were interpolated to the trajectory point using a bilinear interpolation in space. This interpolation scheme is of relatively low order (e.g. Balachander & Maxey 1989), but comparison with higher-order methods showed that owing to the high spatial resolution of the simulation the method is sufficiently accurate. The fluid particles were released at $t/\Delta_t = 5$ and integrated until $t/\Delta_t = 10$. Their initial positions are regularly distributed in a subregion of the computational domain ($2.5 < x_1/L_1 < 3.5$, $1.2 < x_2/L_2 < 2.2$ and $2.5 < x_3/L_3 < 3.5$), in the proximity of the vorticity surface shown in figure 2. The characteristic properties of the experiment and the simulation are summarized in table 1.

3. Results

In both experiment and simulation, turbulence is generated at the plane $x_2 = 0$ and propagates mainly along $x_2 > 0$. In the previous study of Holzner *et al.* (2007) the main focus was on the dependence of small-scale quantities on the distance to the interface. The present investigation concentrates on the analysis of some of
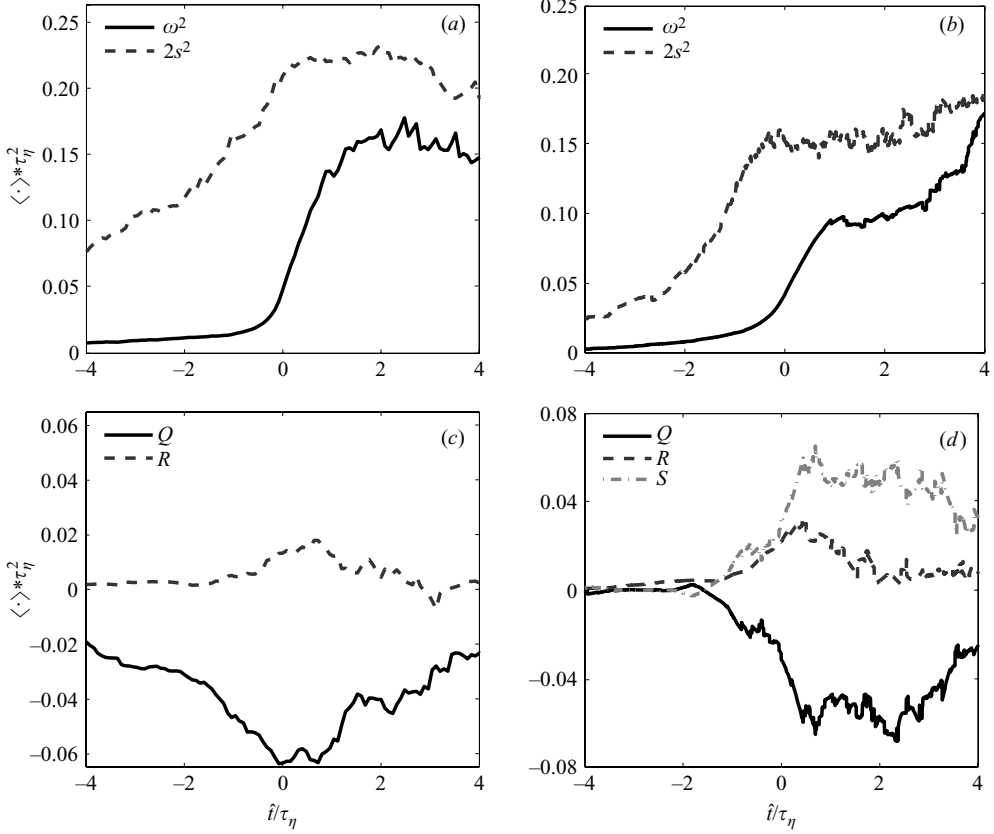
FIGURE 3. Conditionally averaged Lagrangian evolution of ω^2 and $2s^2$ (a, b) and the invariants Q, R and S (c, d), obtained from PTV (left) and DNS (right).

these properties in a Lagrangian frame of reference. We follow fluid tracers initially located in the irrotational region and select particles which at some point cross the turbulent/non-turbulent interface becoming part of the turbulent flow region. For each particle trajectory, the point in time, t^*, when the interface is crossed is identified by using a fixed threshold of enstrophy, $\omega^2 = \omega_i \omega_i$, as in Holzner *et al.* (2006, 2007) and references therein. For details on the selection of the threshold and the effect of its variation see Holzner *et al.* (2007). For the statistical analysis, the measured and simulated particle trajectories are averaged defining an ensemble of events. All trajectories with initial position in the non-turbulent region are centred at the point t^* introduced above and subsequently they are ensemble averaged. For the experiment, about 3×10^3 trajectories with an average length of $4\tau_\eta$ were processed in this way. The number of points considered for the statistics is about 2×10^5. In the simulation, out of the 4×10^3 trajectories about 400 crossed the interface, which yields a total number of 5×10^5 data points.

   Figure 3(a, b) shows the evolution of ω^2 and $2s^2$, as obtained from PTV (a) and DNS (b). The time axis is centred at the point t^*, when the threshold on ω^2 is exceeded, i.e. $\hat{t} = t - t^*$, and normalized by τ_η. We observe that ω^2 is initially very low and increases sharply in the proximity of $\hat{t} = 0$, attaining values of the order of the intensities observed in the turbulent region. The transition from low to high values occurs within a few τ_η. In contrast to enstrophy, strain is already significant in the

non-turbulent region and increases more gradually. A simple argument that partly explains this qualitative difference can be found in Landau & Lifshits (1959, p. 146), which states that in the non-turbulent region vorticity is very small, but strain is not as it consists also of an irrotational part. In the turbulent region, $2\langle s^2 \rangle$ becomes close to $\langle \omega^2 \rangle$, consistent with the results in Holzner *et al.* (2007). The difference in magnitudes between ω^2 and s^2 is an important feature of the observed transition, since in fully developed turbulence enstrophy and strain are 'equal partners' (e.g. Tsinober 2001). If we compare figure 3(a, b) with figure 1 in Holzner *et al.* (2007), it becomes clear that fluid elements pass through an interfacial region with a thickness of a few η, within a time characterized by a few τ_η. This implies that *locally* the characteristic velocity of the fluid relative to the interface is the Kolmogorov velocity, u_η. Figure 3(c, d) illustrates the conditionally averaged evolution of the two invariants of the velocity gradient tensor, $Q = \frac{1}{4}(\omega^2 - 2s^2)$ and $R = -\frac{1}{3}(s_{ij}s_{jk}s_{ki} + \frac{3}{4}\omega_i \omega_j s_{ij})$ and an additional invariant based on the two viscous terms (only DNS), $S = \nu \omega_i \nabla^2 \omega_i - 2\nu s_{ij} \nabla^2 s_{ij}$, as obtained from the experiment (c) and the simulation (d). Apparently, the invariants reach an extremum near $\hat{t}/\tau_\eta = 0$, before they decrease again to lower values. Since the mean values of Q, R and S vanish identically for homogeneous turbulence, their non-zero values indicate that the particle paths cross regions characterized by inhomogeneity, consistent with the analogous results in the form of a distance dependence on the interface location shown in Holzner *et al.* (2007). The agreement between experimental and numerical results is good, at least as far as qualitative trends are concerned. Since the reason for the differences in the evolution of ω^2 and s^2 during the crossing of the interface lies in the different physical processes responsible for their dynamics, in the following we analyse the evolution of the terms of the respective transport equations.

The evolution of the terms of (1.1) is shown in figure 4(a, b) as obtained from PTV (a) and DNS (b). Consistent with the evolution of $\langle \omega^2 \rangle$ shown before, we see that $\langle (D/Dt)\frac{1}{2}\omega^2 \rangle$ is initially low in the irrotational region and grows steeply in the proximity of the interface peaking at $\hat{t} = 0$, before it decreases again on the turbulent side. The viscous term $\langle \nu \omega_i \nabla^2 \omega_i \rangle$ exhibits a peculiar behaviour showing a distinct maximum in the proximity of $\hat{t} = 0$. It appears that initially the major contribution to the growth of ω^2 is due to the viscous term, $\langle \nu \omega_i \nabla^2 \omega_i \rangle > 0$, while the production term $\langle \omega_i \omega_j s_{ij} \rangle$ is small and becomes dominant later. Shortly after the crossing of the interface, $\langle \omega_i \omega_j s_{ij} \rangle$ and $\langle \nu \omega_i \nabla^2 \omega_i \rangle$ balance out, so that $\langle (D/Dt)\frac{1}{2}\omega^2 \rangle$ is small compared to the other terms. It is useful to employ the following decomposition of the term $\nu \omega_i \nabla^2 \omega_i = \nu \nabla^2(\omega^2/2) - \nu \nabla \omega_i : \nabla \omega_i$, where the first term on the right-hand side (the so-called 'viscous diffusion' term) is responsible for the growth of enstrophy at short times, while the second is a (always negative) dissipation term.† The inset in figure 4(b) shows the Lagrangian evolution of the three terms. We note that the term $\nu \nabla^2(\omega^2/2)$ is strongly positive during the process with peak near $\hat{t}/\tau_\eta = 0$, becoming smaller in the turbulent region. On the other hand, the evolution of the negative $\nu \nabla \omega_i : \nabla \omega_i$ is qualitatively similar but remains of comparable magnitude in regions A and B. Figure 4(c, d) shows the evolution of the terms of (1.2) as obtained experimentally (c) and from DNS (d). Compared to the evolution of

---

† Note that the above decomposition of $\nu \omega_i \nabla^2 \omega_i$ – though useful – has a limitation since it is not unique and there is an infinite number of possibilities to represent it as a sum of a dissipation and a flux term (i.e. as a divergence of some vector), e.g. $\boldsymbol{\omega}_i \nabla^2 \omega_i = -(\nabla \times \boldsymbol{\omega})^2 - \nabla \cdot (\boldsymbol{\omega} \times (\nabla \times \boldsymbol{\omega}))$. There is no way to define dissipation (i.e. to choose one among many purely negative expressions) of enstrophy as it is not an inviscidly conserved quantity, unlike the kinetic energy (Tsinober 2001).
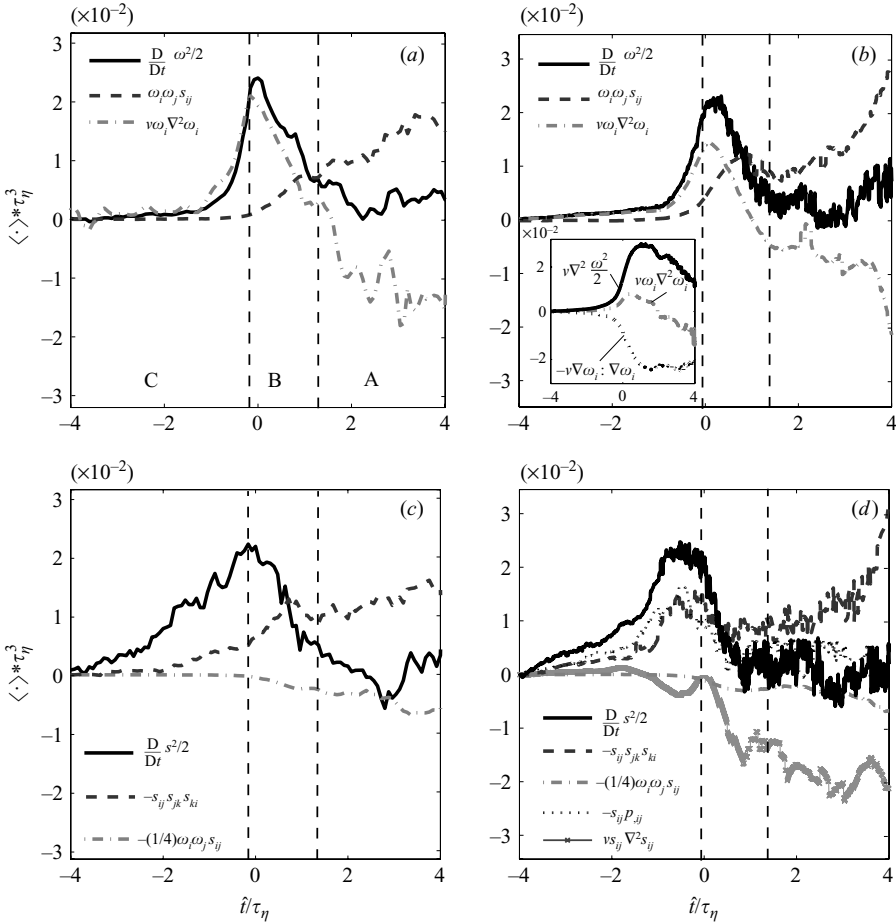
FIGURE 4. Conditionally averaged Lagrangian evolution of the terms of $(1.1)(a, b)$ and $(1.2)(c, d)$ obtained from PTV (left) and DNS (right).

$\langle (D/Dt)\frac{1}{2}\omega^2 \rangle$ observed before, the mean $(D/Dt)\frac{1}{2}s^2$ increases more gradually peaking approximately at $\hat{t} = 0$. As indicated in Holzner *et al.* (2007), we see that the behaviour of strain-related quantities is very different from their vorticity-related counterparts. The contribution to the growth of s^2 is partly due to strain production, $-s_{ij}s_{jk}s_{ki}$, and partly due to the interaction between pressure and strain, $-s_{ij}p_{,ij}$, whereas the viscous term, $\nu s_{ij}\nabla^2 s_{ij}$, is negative in the mean. Unlike $\langle \omega_i\omega_j s_{ij} \rangle$, strain production $-\langle s_{ij}s_{jk}s_{ki} \rangle$ is already significant in the nearly irrotational region and grows anticipating the growth of $\langle \omega_i\omega_j s_{ij} \rangle$. The agreement between numerical and experimental results in figure 4 is not as striking as in figure 3, but the important trends are comparable.

Next, we analyse in more detail to what degree the different quantities contribute to the growth of ω^2 and s^2 during different stages of the process. We apply the convention introduced in Holzner *et al.* (2007) and define three physically distinct regions with respect to the maximum of $\nu\omega_i\nabla^2\omega_i$ (marked in figure 4a): A the *turbulent* region, in which the behaviour of the viscous term is 'normal', i.e. it is negative in the mean; B, the region between the peak and the point where $\langle \nu\omega_i\nabla^2\omega_i \rangle = 0$ is termed the *intermediate* region (with the 'anomalous' viscous production); and C, the *non-turbulent* region
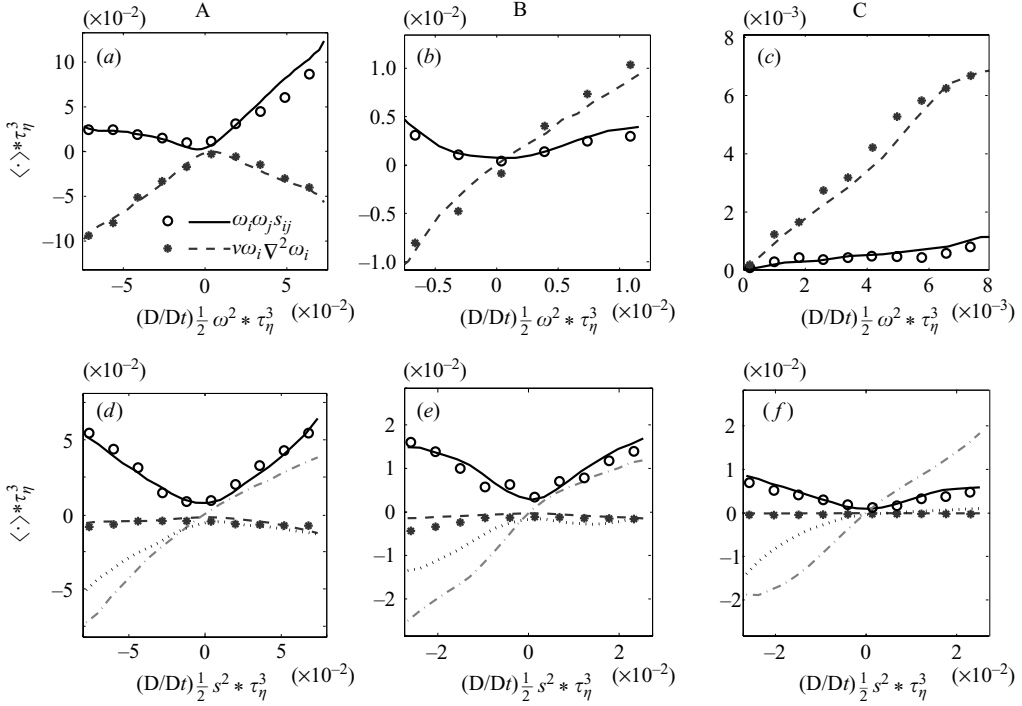
FIGURE 5. Terms on the right-hand side of (1.1) conditioned on $(D/Dt)\frac{1}{2}\omega^2$ $(a–c)$ and terms on the right-hand side of (1.2) conditioned on $(D/Dt)\frac{1}{2}s^2$ $(d–f)$, according to the division in 3 regions shown on figure $4(a)$: turbulent – region A (left), intermediate – region B (centre) and non-turbulent – region C (right). $(d–f)$ $\circ$, —, $-s_{ij}\,s_{jk}\,s_{ki}$; $\bullet$, - - -, $-\frac{1}{4}\omega_i\omega_j\,s_{ij}$; ·—·—, $-s_{ij}p_{,ij}$; ······, $\nu s_{ij}\nabla^2 s_{ij}$. Lines are from DNS, symbols from PTV.

from the peak to $\hat{t}/\tau_\eta = -4$. Figure 5$(a–c)$ shows the terms on the right-hand side of (1.1) conditionally averaged on $(D/Dt)\frac{1}{2}\omega^2$ for the three regions (A–C, from left to right). We see that, on average, in region A inviscid production $(\omega_i\omega_j s_{ij} > 0)$ is the mechanism responsible for the increase of ω^2 and $\nu\omega_i\nabla^2\omega_i$ is negative, whereas negative values of $(D/Dt)\frac{1}{2}\omega^2$ are associated with viscous destruction $(\nu\omega_i\nabla^2\omega_i < 0)$, which counteracts the positive inviscid production. In region B, on average, both inviscid and viscous effects contribute to the increase of ω^2 and, finally, in region C the stronger contributions to the positive $(D/Dt)\frac{1}{2}\omega^2$ are due to $\nu\omega_i\nabla^2\omega_i > 0$. Analogously, figure 5$(d–f)$ shows the terms on the right-hand side of (1.2) conditionally averaged on $(D/Dt)\frac{1}{2}s^2$ for the three regions (A–C, from left to right). Unlike the previous case, the qualitative behaviour changes only weakly throughout regions A–C. In the mean, both the strain production and pressure–strain term contribute strongly to the positive $(D/Dt)\frac{1}{2}s^2$, while the viscous term remains relatively weak. On the other hand, the viscous term and pressure–strain term are in the mean responsible for the decrease of strain, counteracting $-\langle s_{ij}s_{jk}s_{ki}\rangle > 0$. Compared to regions A and B, in region C the positive pressure–strain contribution appears to be somewhat stronger.

Finally, we analyse the dependence of the terms of the two balance equations on the magnitudes of ω^2 and s^2, respectively. Figure 6$(a–c)$ shows the terms of (1.1) conditionally averaged on ω^2 for the three regions (A–C, from left to right). In region A, as expected, for higher values of ω^2, on average $\omega_i\omega_j s_{ij}$ is approximately
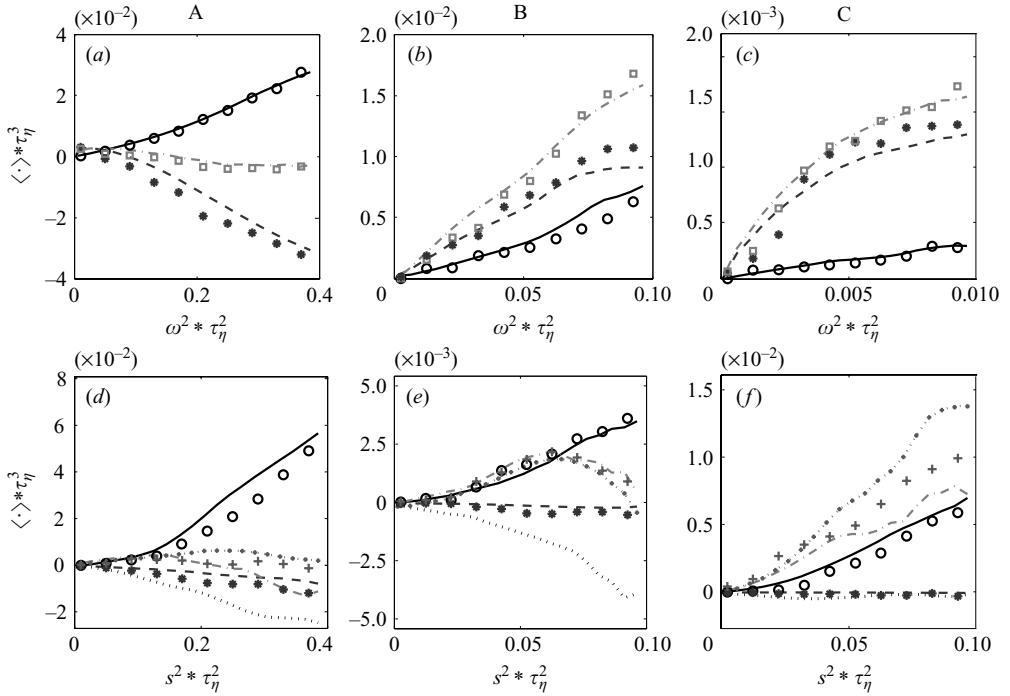
FIGURE 6. Terms of (1.1) conditioned on ω^2 (a–c) and terms of (1.2) conditioned on s^2 (d–f), according to the division in 3 regions: turbulent – region A (left), intermediate – region B (centre) and non-turbulent – region C (right). (a–c) $\bigcirc$, —, $\omega_i \omega_j s_{ij}$; $\bullet$, - - -, $\nu\omega_i \nabla^2 \omega_i$; $\square$, ‑‑‑‑, $(\mathrm{D}/\mathrm{D}t)\frac{1}{2}\omega^2$. ($d$–$f$) $\bigcirc$, —, $-s_{ij}\,s_{jk}\,s_{ki}$; $\bullet$, - - -, $-\frac{1}{4}\omega_i\omega_j s_{ij}$; ‑‑‑‑, $-s_{ij}p_{,ij}$; $\cdots\cdots$, $\nu s_{ij}\nabla^2 s_{ij}$; +, ‑‑‑‑, $(\mathrm{D}/\mathrm{D}t)\frac{1}{2}s^2$. Lines are from DNS, symbols from PTV.

balanced by $\nu\omega_i\nabla^2\omega_i$ so that $(\mathrm{D}/\mathrm{D}t)\frac{1}{2}\omega^2$ is close to zero. For small values of ω^2 we see that the average $(\mathrm{D}/\mathrm{D}t)\frac{1}{2}\omega^2$ is positive due to $\langle\nu\omega_i\nabla^2\omega_i\rangle > 0$, whereas $\langle\omega_i\omega_j s_{ij}\rangle$ is small. In region B, on average both viscous and inviscid effects contribute to a similar degree to the positive $(\mathrm{D}/\mathrm{D}t)\frac{1}{2}\omega^2$, while in region C the viscous contribution dominates. The same analysis for the strain terms is shown in figure 6(d–f). At high levels of s^2, in regions A and B the positive $-\langle s_{ij}s_{jk}s_{ki}\rangle$ is approximately balanced by the other terms so that the average $(\mathrm{D}/\mathrm{D}t)\frac{1}{2}s^2$ is small. At small levels of s^2, both $-\langle s_{ij}s_{jk}s_{ki}\rangle$ and $-\langle s_{ij}p_{,ij}\rangle$ contribute to the positive $\langle(\mathrm{D}/\mathrm{D}t)\frac{1}{2}s^2\rangle$, which is also generally observed in region C. From the behaviour in region A at low intensities we see that the characteristics in the proximity of interfaces might be similar to the dominating small-scale mechanisms observed in regions characterized by low levels of strain and enstrophy in fully developed turbulence.

4. Conclusions

In summary, a Lagrangian study was carried out to investigate small-scale properties of the mechanism of turbulent entrainment through 3D-PTV and DNS. The experimental results are in good agreement with the simulation, at least on a qualitative level, which is considered as a clear indication for the reliability of both methods. We found that the entrainment mechanism is characterized by a sequence of events. The process starts with amplification of s^2 through the combined

effect of strain production and pressure–strain interaction. Next, a sharp increase of ω^2 induced mostly by $\nu\omega_i\nabla^2\omega_i > 0$ is observed, followed by a gradual increase of enstrophy production $\omega_i\omega_j s_{ij}$ and the change of sign of $\nu\omega_i\nabla^2\omega_i$. Finally, production and dissipation of both enstrophy and strain come to a balance. There is an indication that a similar sequence might be observed also in regions initially characterized by low levels of strain and enstrophy in fully developed turbulence. The analysis substantiates that locally the characteristic velocity of the fluid relative to the turbulent/non-turbulent interface is the Kolmogorov velocity, u_η.

REFERENCES

BALACHANDAR, S. & MAXEY, M. R. 1989 Methods for evaluating fluid velocities in spectral simulations of turbulence. *J. Comput. Phys.* **83**, 96–125.

BISSET, D. K., HUNT, J. C. R. & ROGERS, M. M. 2002 The turbulent/non-turbulent interface bounding a far wake. *J. Fluid Mech.* **451**, 383–410.

CORRSIN, S. 1943 Investigation of flow in an axially symmetric heated jet in air. *NACA* ACR 3L23 and *Wartime Rep.* W94.

CORRSIN, S. & KISTLER, A. L. 1954 The free-stream boundaries of turbulent flows. *NACA* TN-3133, TR-1244, pp. 1033–1064.

HOLZNER, M., LIBERZON, A., GUALA, M., TSINOBER, A. & KINZELBACH, W. 2006 An experimental study on the propagation of a turbulent front generated by an oscillating grid. *Exps. Fluids* **41**, 711–719.

HOLZNER, M., LIBERZON, A., NIKITIN, N., KINZELBACH, W. & TSINOBER, A. 2007 Small scale aspects of flows in proximity of the turbulent/non-turbulent interface. *Phys. Fluids* **19**, 071702.

HOYER, K., HOLZNER, M., LÜTHI, B., GUALA, M., LIBERZON, A. & KINZELBACH, W. 2005 3D scanning particle tracking velocimetry. *Exps. Fluids* **39**, 923–934.

HUNT, J. C. R., EAMES, I. & WESTERWEEL, J. 2006 Mechanics of inhomogeneous turbulence and interfacial layers. *J. Fluid Mech.* **554**, 449–519.

LANDAU, L. D. & LIFSHITS, E. M. 1959 *Fluid Mechanics.* Pergamon.

LÜTHI, B., TSINOBER, A. & KINZELBACH, W. 2005 Lagrangian measurement of vorticity dynamics in turbulent flow. *J. Fluid Mech.* **528**, 87–118.

MATHEW, J. & BASU, A. J. 2002 Some characteristics of entrainment at a cylindrical turbulence boundary. *Phys. Fluids* **14**, 2065–2072.

MORDANT, N., CRAWFORD, A. M. & BODENSCHATZ, E. 2004 Experimental Lagrangian acceleration probability density function measurement. *Physica* D, **193**, 245–251.

NIKITIN, N. 2006 Finite-difference method for incompressible Navier-Stokes equations in arbitrary orthogonal curvilinear coordinates. *J. Comput. Phys.* **217**, 759–781.

OTT, S. & MANN, J. 2000 An experimental investigation of the relative diffusion of particle pairs in three-dimensional turbulent flow. *J. Fluid Mech.* **422**, 207–223.

POULAIN, C., MAZELLIER, N., GERVAIS, P., GAGNE, Y. & BAUDET, C. 2004 Spectral vorticity and Lagrangian velocity measurements in turbulent jets. *Flow, Turb. Combust.* **72**, 245–271.

TRITTON, D. J. 1988 *Physical Fluid Dynamics* 2nd edn. Clarendon.

TSINOBER, A. 2001 *An Informal Introduction to Turbulence.* Springer.

VOTH, G. A., LA PORTA, A., CRAWFORD, A. M., ALEXANDER, J. & BODENSCHATZ, E. 2002 Measurement of particle accelerations in fully developed turbulence. *J. Fluid Mech.* **469**, 121–160.

WESTERWEEL, J., FUKUSHIMA, C., PEDERSEN, J. M. & HUNT, J. 2005 Mechanics of the turbulent/non-turbulent interface of a jet. *Phys. Rev. Lett.* **95**, 174501.

WESTERWEEL, J., HOFFMANN, T., FUKUSHIMA, C. & HUNT, J. C. R. 2002 The turbulent/non-turbulent interface at the outer boundary of a self-similar turbulent jet. *Exps. Fluids* **33**, 873–878.